

LJMU Research Online

Maccary, R, Guidorzi, C, Camisasca, AE, Maistrello, M, Kobayashi, S, Amati, L, Bazzanini, L, Bulla, M, Ferro, L, Frontera, F and Tsvetkova, A

Gamma-ray burst minimum variability timescales with Fermi/GBM

https://researchonline.ljmu.ac.uk/id/eprint/27360/

Article

Citation (please note it is advisable to refer to the publisher's version if you intend to cite from this work)

Maccary, R ORCID logoORCID: https://orcid.org/0000-0002-8799-2510, Guidorzi, C ORCID logoORCID: https://orcid.org/0000-0001-6869-0835, Camisasca, AE ORCID logoORCID: https://orcid.org/0000-0002-4200-1947, Maistrello. M ORCID logoORCID: https://orcid.org/0009-0000-4422-4151.

LJMU has developed LJMU Research Online for users to access the research output of the University more effectively. Copyright © and Moral Rights for the papers on this site are retained by the individual authors and/or other copyright owners. Users may download and/or print one copy of any article(s) in LJMU Research Online to facilitate their private study or for non-commercial research. You may not engage in further distribution of the material or use it for any profit-making activities or any commercial gain.

The version presented here may differ from the published version or from the version of the record. Please see the repository URL above for details on accessing the published version and note that access may require a subscription.

For more information please contact researchonline@ljmu.ac.uk



Gamma-ray burst minimum variability timescales with Fermi/GBM

R. Maccary^{1,2,*}, C. Guidorzi^{1,2,3}, A. E. Camisasca^{8,1}, M. Maistrello^{1,2}, S.Kobayashi⁷, L. Amati², L. Bazzanini^{1,2}, M. Bulla^{1,3,4}, L. Ferro ^{1,2}, F. Frontera^{1,2}, and A. Tsvetkova^{5,6}

- Department of Physics and Earth Science, University of Ferrara, Via Saragat 1, I-44122, Ferrara, Italy
- ² INAF Osservatorio di Astrofisica e Scienza dello Spazio di Bologna, Via Piero Gobetti 101, I-40129 Bologna, Italy
- ³ INFN Sezione di Ferrara, Via Saragat 1, I–44122, Ferrara, Italy
- ⁴ INAF, Osservatorio Astronomico d'Abruzzo, Via Mentore Maggini snc, 64100 Teramo, Italy
- ⁵ Department of Physics, University of Cagliari, SP Monserrato-Sestu, km 0.7, 09042 Monserrato, Italy
- ⁶ Ioffe Institute, Politekhnicheskaya 26, 194021 St. Petersburg, Russia
- Astrophysics Research Institute, Liverpool John Moores University, Liverpool Science Park IC2, 146 Brownlow Hill, Liverpool L3 5RF, UK
- 8 Alma Mater Studiorum, Università di Bologna, Dipartimento di Fisica e Astronomia (DIFA), Via Gobetti 93/2, 40129 Bologna, Italy

Received 7 May 2025 / Accepted 10 August 2025

ABSTRACT

Context. Gamma-ray bursts (GRBs) have traditionally been classified by duration as long (LGRBs) or short (SGRBs), with the former believed to originate from massive star collapses and the latter from compact binary mergers. However, events such as the SGRB 200826A (coming from a collapsar) and the LGRBs 211211A and 230307A (associated with a merger) suggest that duration-based classification could sometimes be misleading. Recently, the minimum variability timescale (MVT) has emerged as a key metric for classifying GRBs.

Aims. We calculated the MVT, defined as the full width at half maximum (FWHM) of the narrowest pulse in the light curve, using an independent dataset from Fermi/GBM, and we compared our results with other MVT definitions. We updated the MVT- T_{90} plane and analysed peculiar events such as long-duration merger candidates 211211A, 230307A, and other short GRBs with extended emission (SEE-GRBs). We also examined extragalactic magnetar giant flares (MGFs) and explored possible new correlations with peak energy. Methods. We used the MEPSA algorithm to identify the shortest pulse in each GRB light curve and measured its FWHM. We calculated the MVT for around 3700 GRBs, 177 of which have spectroscopically known redshift.

Results. The SEE-GRBs and SGRBs share similar MVTs (from a few tens of to a few hundred milliseconds, indicating a common progenitor, while extragalactic MGFs exhibit even shorter values (from a few milliseconds to a few tens of milliseconds). Our MVT estimation method consistently yields higher values than another existing technique, the latter aligning with the pulse rise time. For LGRBs, we confirm the correlations of MVT with peak luminosity and Lorentz factor.

Conclusions. We confirm that although MVT alone cannot determine the GRB progenitor, it is a valuable tool when combined with other indicators, as it helps flag long-duration mergers and distinguish MGFs from typical SGRBs.

Key words. methods: statistical – gamma-ray burst: general

1. Introduction

Gamma-ray bursts (GRBs) are brief yet extremely intense flashes of gamma rays produced at cosmological distances. They are thought to arise from at least two types of catastrophic events: (i) the core-collapse of certain types of massive star, known as collapsars (Woosley 1993; Paczyński 1998; MacFadyen & Woosley 1999; Yoon & Langer 2005) – typically occurring at the centre of star-forming galaxies (Fruchter et al. 2006) and associated with Type Ic-BL supernovae (Galama et al. 1998; Hjorth et al. 2003), and (ii) binary compact object mergers (Blinnikov et al. 1984; Paczynski 1986; Eichler et al. 1989; Paczynski 1991; Narayan et al. 1992; Abbott et al. 2017). The central engine, which powers an ultra-relativistic jet, could be either a stellar-mass black hole surrounded by a hyper-accreting thick accretion disc (Popham et al. 1999; Di Matteo et al. 2002; Janiuk et al. 2007; Lei et al. 2013) or a strongly magnetised,

rapidly spinning neutron star, also known as a magnetar (Usov 1992; Wheeler et al. 2000; Thompson et al. 2004; Metzger et al. 2011). Despite much progress, the exact nature of the central engine(s), the mechanism(s) by which the relativistic jet is launched, the jet composition, and the radiation process(es) responsible for the gamma-ray emission remain unresolved questions.

Initially, GRBs were classified by their duration, with long GRBs (LGRBs) typically linked to collapsars and short GRBs (SGRBs) to mergers. However, a class of events known as SGRBs with extended emission (SEE-GRBs) and presenting a short, hard spike followed by a longer softer emission (sometimes lasting tens of seconds) challenged this simple classification (Norris & Bonnell 2006). For instance, events such as 060614 (Gehrels et al. 2006; Della Valle et al. 2006; Fynbo et al. 2006; Jin et al. 2015; Yang et al. 2015), which exhibited zero spectral lag and no evidence of a supernova despite occurring at low redshift, raised doubts about the reliability of using duration alone to infer the kind of progenitor. In many cases, the

^{*} Corresponding author: mccrnl@unife.it

host galaxy remains undetected, and redshift measurements are unavailable, making it difficult to determine the progenitor type. Recent cases, such as 211211A ($T_{90} \simeq 34$ s; Rastinejad et al. 2022; Gompertz et al. 2023; Yang et al. 2022; Troja et al. 2022; Xiao et al. 2022) and 230307A ($T_{90} \simeq 35$ s; Dalessi et al. 2023; Xiong et al. 2023; Du et al. 2024; Dai et al. 2024; Levan et al. 2024; Yang et al. 2024) were followed by a kilonova (KN), which provided compelling evidence that even mergers can produce long-duration GRBs, further emphasising the need for a new classification system. Given the growing complexity, families (i) and (ii) are now frequently described as merger GRBs and collapsar GRBs or, alternatively, as Type-I and Type-II GRBs, respectively (Zhang 2006).

Among fast, high-energy transient events, there is another category known as magnetar giant flares (MGFs), which is sometimes mistaken for typical SGRBs. These events, produced by galactic or extragalactic magnetars, are characterised by a shorter rise time and duration, a harder peak energy, and a lower equivalent-isotropic energy, $E_{\rm iso} \approx 10^{44-46}$ erg, compared to cosmological SGRBs. When occurring within the Milky Way, they exhibit a long decaying tail modulated by the neutron star rotation period (Mazets et al. 1979; Feroci et al. 1999; Hurley et al. 1999, 2005), which is below instrumental sensitivity when they happen in nearby galaxies (Ofek et al. 2006; Mazets et al. 2008; Burns et al. 2021; Svinkin et al. 2021; Roberts et al. 2021; Fermi-Lat Collaboration 2021; Mereghetti et al. 2024; Trigg et al. 2024; Rodi et al. 2025).

Numerous attempts to classify GRBs using different prompt emission properties have been made (Goldstein et al. 2010; Lü et al. 2010, 2014; Tsvetkova et al. 2025). Many efforts have also been made to develop machine-learning (ML) based GRB classification methods (Jespersen et al. 2020; Salmon et al. 2022; Steinhardt et al. 2023; Dimple et al. 2023; Garcia-Cifuentes et al. 2023; Chen et al. 2024; Zhu et al. 2024; Dimple et al. 2024). These methods generally recover the usual properties of the two GRB classes. ML-identified Type I GRBs tend to be shorter and spectrally harder than ML-identified Type II GRBs. However, complex cases – such as GRB 211211A and GRB 230307A - continue to challenge even the most advanced classification algorithms (see e.g. Zhu et al. 2024). This highlights the persistent challenges in GRB classification and the importance of identifying the most relevant parameters for distinguishing GRB progenitors. A promising approach involves the minimum variability timescale (MVT), defined as the shortest timescale over which the signal shows uncorrelated temporal variability. Several methods have been proposed to calculate the MVT, such as temporal deconvolution into pulses (Norris et al. 1996, 2005; Bhat et al. 2012) and wavelet decomposition (MacLachlan et al. 2013; Golkhou & Butler 2014; Golkhou et al. 2015; Vianello et al. 2018).

The MVT could be directly linked to the activity of the central engine, as is the case for the internal shock (IS) model (Rees & Meszaros 1994; Kobayashi et al. 1997; Daigne & Mochkovitch 1998), or it may originate locally in the emission region. In the latter case, either relativistic turbulence (Kumar & Narayan 2009) or the emission of Doppler-boosted local emitters (Lyutikov et al. 2003) could determine the MVT. These two pictures are being unified by the Internal Collision-Induced Magnetic Reconnection and Turbulence model (ICMART; Zhang & Yan 2011), according to which longer timescales are linked to the central engine activity, while the shorter ones are attributed to relativistic magnetic turbulence within the emission region.

Camisasca et al. (2023a, hereafter C23) defined the MVT as the full width half maximum (FWHM) of the shortest pulse that is detected with statistical confidence within a GRB light curve (LC). This method builds on the MEPSA algorithm (Guidorzi 2015), which was designed to identify statistically significant peaks in a given GRB LC. This method has the advantage of having a straightforward interpretation. In their study, they explored various possible correlations between the MVT, Lorentz factor, jet opening angle, and peak luminosity.

This method was also applied to the case of 230307A, where an MVT of 28 ms was reported by Camisasca et al. (2023b), suggesting a merger origin, in agreement with the discovery of a KN (Bulla et al. 2023; Levan et al. 2024). This confirms the usefulness of the MVT in identifying long-duration merger candidates. The MVT can also be useful in distinguishing extragalactic MGFs from regular SGRBs.

The combination of MVT and other metrics may help further identify interesting merger candidates. In fact, Guidorzi et al. (2024a) showed that the combination of high variability (V > 0.1), relatively low luminosity $L_{\rm iso} < 10^{51}$ erg s⁻¹, and short MVT (≤ 0.1 s) may be indicative of a compact binary merger origin, in spite of the long duration and misleading temporal profile.

Our goal is to verify the results obtained by C23 using the complementary dataset of the *Fermi* Gamma-ray Burst Monitor (GBM; Meegan et al. 2009). This is an all-sky monitor, and it is sensitive to soft gamma-rays, with 12 sodium iodide (NaI) scintillators working in the range from 8 to 1000 keV and two additional bismuth germanate (BGO) detectors operating from 150 keV to 30 MeV.

On the one hand, it is important to test the results obtained by C23 through an independent dataset. On the other hand, the GBM data in particular allow us to update and extend the analysis to interesting candidates that were detected exclusively with GBM. With over 3000 recorded GRBs, excellent time resolution (<10 μs), and its large energy passband, Fermi/GBM is ideally suited to a statistical analysis of GRB MVTs.

We have organized this work as follows: Section 2 describes the GRB sample and the data analysis. Results are reported in Section 3. We discuss the implications and conclude in Section 4. Hereafter, we use the flat- Λ CDM cosmology model with the latest cosmological parameters values $H_0 = 67.66$ km Mpc⁻¹ s⁻¹ and $\Omega_0 = 0.31$ (Planck Collaboration VI 2020).

2. Data analysis

2.1. Dataset

We started with 3792 GRBs triggered by Fermi/GBM from 14 July 2008 to 11 June 2024. We kept 3720 of them, as the others were not entirely covered by time tagged events (TTE) data. Some very bright GRBs, such as 221009A and 130427A, were also removed due to their brightness, which saturated the NaI detectors (Ackermann et al. 2014; Lesage et al. 2023). Among the remaining GRBs, 177 have a measured redshift, with 152 classified as collapsar candidates (or Type-II), 20 as merger candidates (or Type-I), and 5 as SEE-GRBs. Seventeen GRBs of the former class are associated with a supernova (SN). We also have 44 SEE-GRBs, either identified by Kaneko et al. (2015), Lien et al. (2016), Lan et al. (2020) or reported as such by the Gamma-ray Coordinate Network. Additionally, two longduration merger candidates, 211211A and 230307A, appear in our sample. They are LGRBs, having $T_{90} > 2$ s, and do not necessarily follow the morphology of SEE-GRBs. Table 1 reports the data.

Table 1. First five GRBs of our sample. This table is available in its entirety in machine-readable form (see Section 5).

GRB	Fermi Id	FWHM _{min} [s]	T ₉₀ [s]	z	N _p	Туре
080714B	bn080714086	$2.429^{+0.848}_{-0.628}$	5.376	_	2	II
080714C	bn080714425	$5.387^{1.880}_{-1.393}$	40.192	-	2	II
080714A	bn080714745	$3.825_{-0.990}^{1.335}$	59.649	-	1	II
080715	bn080715950	$0.172^{0.060}_{-0.045}$	7.872	_	2	II
080717	bn080717543	$7.252^{2.532}_{-1.876}$	36.608	-	1	II

Table 2. Three MGFs in our sample.

GRB	Fermi Id	FWHM _{min} [ms]	T ₉₀ [s]	d [Mpc]
180128A	bn180128215	$8.12^{+2.80}_{-2.1}$	0.208	3.7
200415A	bn200415367	$2.97^{+1.04}_{-0.77}$	0.144	3.5
231115A	bn231115650	$24.41^{+8.52}_{-6.31}$	0.032	3.5

We also considered three extragalactic MGFs: 200415A (Yang et al. 2020; Roberts et al. 2021; Svinkin et al. 2021; Fermi-Lat Collaboration 2021), 231115A (Mereghetti et al. 2024; Minaev et al. 2024), and 180128A (Trigg et al. 2024). Their data are reported in Table 2.

2.2. Data reduction

We used the TTE data in the 8–1000 keV energy range, with an integration time of 64 ms. Whenever it was required by the procedure described in C23, we also used 1024, 4, and 1 ms. For each burst, we selected the GBM detectors based on the 'bcat detector mask' entry in the HEASARC catalogue¹. We discarded the GRBs affected by solar flares and those with profiles not entirely contained in the TTE mode of GBM. The background was interpolated and subtracted using the GBM data tools² (Goldstein et al. 2022) and following the standard procedures also applied in Maccary et al. (2024).

2.3. Minimum variability timescale computation

We adopted the MVT calculation defined in C23 as the FWHM of the narrowest, statistically significant peak in the LC (denoted hereafter as FWHM_{min}). We measured FWHM_{min} following the prescriptions of C23, which build upon MEPSA:

- The MVT is tentatively computed on the 64 ms LC, and the binning scheme is refined down to 4 ms or even 1 ms when needed.
- MEPSA is applied to the corresponding LCs, using a maximum rebin factor of 256.
- Peaks are filtered using S/N thresholds following a scheme ensuring the same false alarm probability through different bin times³ (see Figure 1 of C23).
- The FWHM of each peak is computed using the calibrated formula established in C23, which depends on MEPSA

parameters. Then, the FWHM of the shortest significant peak is defined as $FWHM_{min}$.

We compared the results of this method with a more direct computation of the FWHM of the shortest significant pulse obtained by fitting its time profile with a fast rise exponential decay (FRED) model (see Appendix A for more details). In Appendix B, we present a comparison of the results obtained using *Swift*/BAT and *Fermi*/GBM data. Also, in Appendix C we compare the results of our method with those obtained with the Bayesian blocks (Scargle et al. 2013) algorithm.

Out of 3720 GRBs, we obtained 3350 GRBs with a reliable measure of FWHM_{min}. Of these, 2992 of them are LGRBs ($T_{90} > 2$ s), while 358 are SGRBs ($T_{90} < 2$ s). For 29 GRBs, we could only determine an upper limit of FWHM_{min}. For 339 GRBs, the S/N was not high enough to enable a reliable measure of FWHM_{min}.

3. Results

In the following, we present the results of the MVT measurements for the 3350 GRBs for which FWHM $_{\rm min}$ was successfully determined. We analyse the distribution of MVT of different GRB classes, examine correlations with other burst properties, and compare these findings with models and former studies.

3.1. Comparison between our MVT estimation with other techniques

We compared three possible ways to measure the MVT: (i) the FWHM of the narrowest pulse, denoted as FWHM_{min}; (ii) the MVT as computed by Golkhou et al. (2015, hereafter G15) and Veres et al. (2023, hereafter V23) using wavelet decomposition, denoted as $\Delta t_{\rm min}$; and (iii) the detection timescale of the narrowest pulse identified by MEPSA, denoted as $\Delta t_{\rm det}$, which is the time interval over which the detection significance is maximised (see Guidorzi 2015 for details). The FWHM_{min} can be computed either by directly fitting the LC or by using MEPSA along with the procedure described in Sect. 2.3. As demonstrated in Appendix A, the two methods give similar results, with most estimates compatible within uncertainties. Therefore, for the purpose of (i), we only consider the latter approach, as it gives a reliable estimate of the narrowest pulse FWHM.

Figure 1 compares FWHM_{min} and Δt_{min} . We observed a significant discrepancy between the two, with FWHM_{min} being significantly longer. Interestingly, the Δt_{min} values are consistent with the detection timescale values Δt_{det} calculated by MEPSA (Figure 2).

According to simulations carried out in Guidorzi (2015) and C23, the brighter the pulse, the smaller the ratio of $\Delta t_{\rm det}$ /FWHM. Specifically, C23 came up with a calibrated relation between FWHM_{min} and $\Delta t_{\rm det}$, which they used to estimate the former from the latter while also using other ancillary information yielded by MEPSA and modelling the corresponding uncertainty (see Equation A3 therein).

Our analysis confirms that $\Delta t_{\rm min}$ is more closely related with the detection timescale (Figure 2) and the rise time, t_r (Figure 3), than the FWHM (Figure 1) of the pulse, as also mentioned by G15. Indeed, $\Delta t_{\rm det} \sim \Delta t_{\rm min} \sim t_r$, with median values of 0.6 and 1.1 for $\Delta t_{\rm det}/\Delta t_{\rm min}$ and $\Delta t_{\rm min}/t_r$, respectively. The GRB pulses are typically asymmetric, with a decay-to-rise time ratio of 3–4. As a consequence, the FWHM is comparably longer than the rise time alone and explains why FWHM_{min} is longer than $\Delta t_{\rm min}$ by a comparable factor. This difference between FWHM_{min} and

https://heasarc.gsfc.nasa.gov/db-perl/W3Browse/
w3table.pl?tablehead=name%3Dfermigbrst&Action=More+
Options

https://fermi.gsfc.nasa.gov/ssc/data/analysis/gbm/
gbm_data_tools/gdt-docs/.

³ S/N \geq 7, 6.8, 6.4, 6 at 1, 4, 64, 1024 ms.

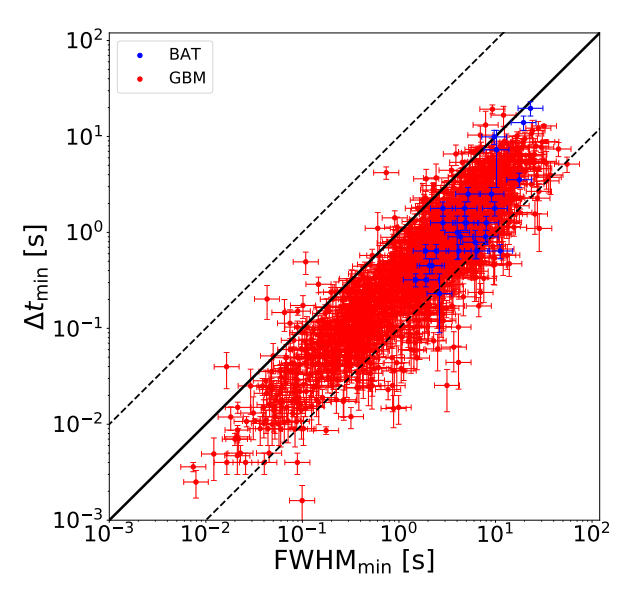


Fig. 1. Plot representing $\Delta t_{\rm min}$ versus FWHM_{min} for the GRBs in common. Red points show GBM data, where $\Delta t_{\rm min}$ was taken from G15 and V23, while blue points are BAT data, with $\Delta t_{\rm min}$ being taken from Golkhou & Butler (2014). Equality is shown with a solid line, while dashed lines show ± 1 dex.

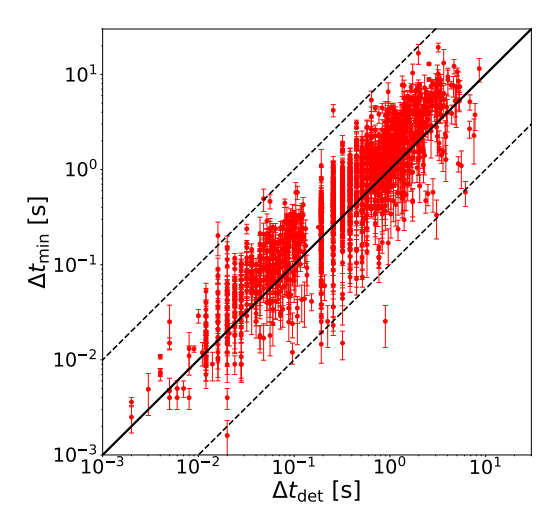


Fig. 2. Plot representing $\Delta t_{\rm min}$ versus $\Delta t_{\rm det}$ for the GRBs in common. $\Delta t_{\rm min}$ is the MVT estimate from G15 and V23 obtained with GBM, while $\Delta t_{\rm det}$ is the detection timescale found with MEPSA. Solid and dashed lines have the same meaning as in Figure 1.

 Δt_{\min} is important to bear in mind, especially when it is to be interpreted within a theoretical context.

3.2. FWHM_{min}-T₉₀ plane

Following C23, in Figure 4 we plot FWHM_{min} versus T_{90} for the bursts of our sample. We also computed the median value of FWHM_{min} for the various GRB classes and applied two-population Kolmogorov-Smirnov (KS) tests to investigate their mutual compatibility. Results are reported in Table 3. Clearly, LGRBs show greater FWHM_{min} values, with a median value of 2.4 s, while it is about 0.2 s for the SGRBs. The GRBs with an ascertained SN association have typical FWHM_{min} values similar to the bulk of LGRBs, with a median value of about 1.6 s,

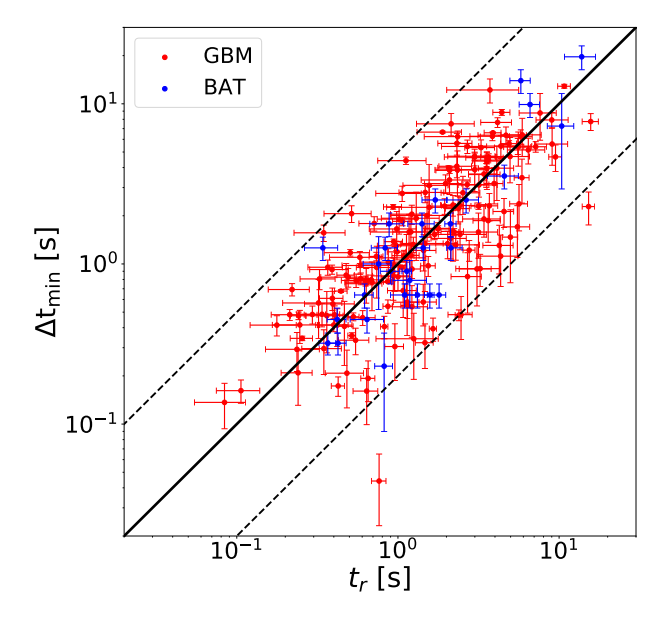


Fig. 3. Plot showing Δt_{\min} versus the rise time t_r of the fitted pulse for the samples of GRBs defined in Appendix A. Red points show GBM data, where Δt_{\min} was taken from G15 and V23, while blue points are BAT data, with Δt_{\min} taken from Golkhou & Butler (2014). The solid and dashed lines have the same meaning as in Figure 1.

thus pointing towards a common collapsar origin for the bulk of LGRBs.

Conversely, SEE-GRBs FWHM_{min} values (about 0.15 s) are closer to those of SGRBs than LGRBs, supporting a common origin. Our results are consistent with those of Kaneko et al. (2015) and Lan et al. (2020). Among them, 161129A was also noted by Guidorzi et al. (2024a) to have a combination of high variability $V \sim 0.6$, relatively low luminosity ($L_p \sim 2 \times 10^{51}$ erg s⁻¹), and short MVT, which is potentially characteristic of long-duration merger candidates. The initial spike has an MVT of about 20 ms, although it is slightly below the threshold detection of our technique, having SNR_{4ms} = 6.6 < SNR_{4ms} = 6.8 for the 4 ms binned LC.

Long-duration merger candidates, such as 211211A and 230307A, are definite outliers in the LGRB FWHM_{min} distribution, with an MVT of 5 and 17 ms, respectively. These two cases show that duration alone could be misleading and showcase the potential of MVT to unveil these baffling merger candidates, as already pointed out in C23 and V23. Notably, 2% of LGRBs have FWHM_{min} ≤ 0.1 s, indicating that LGRBs could include unidentified merger candidates. A few of these events, which also look similar to canonical SEE-GRBs, are displayed in Figure 5. Additionally, we considered 191019A, a long GRB $(T_{90} = 64 \text{ s})$ at redshift z = 0.248 and with no associated SN, which might also be a merger candidate (Levan et al. 2023; Stratta et al. 2025). We note that 191019A was not detected by GBM; however, using Swift/BAT data, Camisasca et al. (2023a) reported an MVT of 0.196 s. Assuming the scaling of FWHM_{min} with photon energy (see Appendix D), we estimated that we would have found 0.14 – 0.15 s with the GBM, placing 191019A in the outskirts of the LGRB FWHM $_{min}$ distribution. 221009A is not included in this analysis, owing to the strong saturation issues in Fermi/GBM. A MVT of 0.1 s, obtained with HXMT/HE data, was reported by Zhang et al. (2025), compatible with both Type I and II FWHM_{min} distributions.

The MGFs have a mean FWHM_{min} of 12 ms, hence exhibiting even shorter values than typical SGRBs. Table 3 shows the

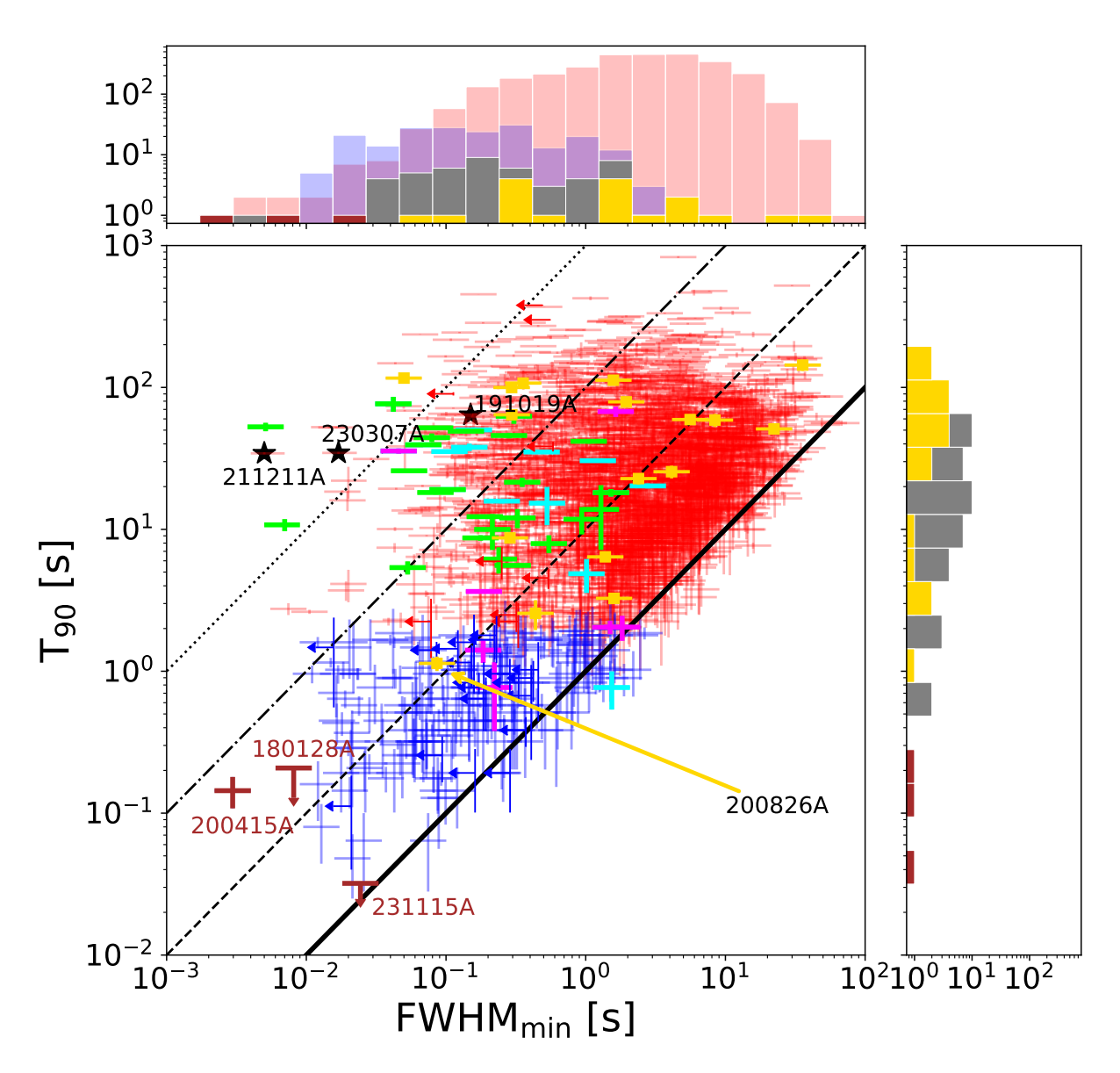


Fig. 4. Scatter plot of FWHM_{min} and T_{90} for the *Fermi/GBM* sample along with the corresponding marginal distributions. Blue (red) points represent short (long) GRBs. Gold points represent SN-associated GRBs. Magenta, lime, and cyan points represent SEE-GRBs from Lien et al. (2016), Lan et al. (2020), Kaneko et al. (2015), respectively. Three extragalactic MGFs candidates, 180128A, 200415A, and 231115A, are shown in brown. The SEE-GRBs from the three samples considered are shown altogether in grey in the top and right panel. We also show with a black star the two peculiar LGRBs, 211211A and 230307A, associated with a kilonova event and 191019A, which may be a short GRB that exploded in a dense environment. We also highlight the peculiar short collapsar GRB 200826A associated with an SN.

median $FWHM_{min}$ value for the different populations as well as the result of the KS tests.

3.3. Peak rate versus FWHM_{min}

In line with the procedure of C23, we characterised the detection efficiency of MEPSA applied to GBM data as a function of both FWHM_{min} and PR_{max}, the latter being the maximum peak rate of any given pulse. To this aim, we generated synthetic pulses assuming the Norris function (Norris et al. 1996) and added a constant background with a count rate selected from a sample of real background rates observed with GBM. For each GRB, the background rate is the sum of the individual rates across all the NaI detectors involved. Poisson noise was finally simulated for the total expected counts per bin. We simulated GRBs with PR_{max} ranging from 10^2 to 10^5 cts s $^{-1}$ and with FWHM_{min} going

from 10^{-2} to 10^2 s. For each point of this grid, we simulated 100 pulses and estimated the detection efficiency by counting how many times MEPSA detected the peak with a S/N > 5. The detection efficiency, $\epsilon_{\rm det}$, is approximately described by a linear function of the logarithm of both quantities:

$$\epsilon_{\text{det}} = a \log_{10} \left(\frac{\text{FWHM}_{\text{min}}}{\text{s}} \right) + b \log_{10} \left(\frac{\text{PR}_{\text{max}}}{\text{cts s}^{-1}} \right) + c. \tag{1}$$

The optimal coefficients were found to be a=1.27, b=2.83, and c=-7.33. Eq. (1) is the GBM analogous of Eq. (2) of C23:

$$PR_{max} \ge 877 \text{ cts s}^{-1} \left(\frac{FWHM_{min}}{s}\right)^{-0.45} 10^{0.35(\epsilon-1)}.$$
 (2)

The meaning of Eq. (2) is illustrated by the following example: For a pulse with MVT of 10 ms to be correctly identified with

Table 3. Median FWHM_{min} values for different GRB groups along with the p-values of the two-population KS test between the FWHM_{min} values of each corresponding pair of groups.

Sample	FWHM _{min} (s)	LGRBs	SGRBs
LGRBs (2994)	2.4	_	$10^{-69} (\times)$
SN GRBs (17)	1.6	0.17 (🗸)	$7.1\ 10^{-5}\ (\times)$
SGRBs (358)	0.15	$10^{-69} (\times)$	_
SEE-GRBs ^(b) (6)	0.11	0.0004 (×)	0.73 (🗸)
SEE-GRBs ^(c) (16)	0.16	$7.5 \ 10^{-5} \ (\times)$	0.75 (🗸)
SEE-GRBs ^(d) (22)	0.2	$1.3 \ 10^{-12} \ (\times)$	0.73 (🗸)
MGFs (e) (3)	0.008	$2.3 \ 10^{-7} \ (\times)$	0.003 (×)

Notes. ^(a)Median value. ^(b)Identified by Lien et al. (2016). ^(c)Identified by Kaneko et al. (2015). ^(d)Identified by from Lan et al. (2020). ^(e)From extragalactic magnetars.

90% confidence, its peak rate has to be \gtrsim 6430 cts s⁻¹ (a condition that is fulfilled by just 13% of the bursts in our sample). Figure 6 illustrates ϵ_{det} in the PR_{max}-FWHM_{min} plane.

3.4. Peak luminosity versus FWHM_{min}

We computed the isotropic-equivalent peak luminosities, $L_{\rm p}$, as done in Maccary et al. (2024) for 152 collapsar-candidate GRBs with known redshift. We studied the L_p – FWHM_{min} correlation, which was observed in other catalogues (C23). The result is shown in Figure 7.

The selection effects significantly influence the distribution in the L_p -FWHM_{min} plane. Specifically, narrower pulses require a higher peak rate to be detected. This selection bias could hide possible weak and short bursts that could contribute to demote the correlation. To account for this bias, we carried out a suite of simulations following the procedure set up in C23. We divided our sample into nine bins of redshift and simulated points within the L_p – FWHM_{min} plane for each bin. For each bin, we randomly generated as many points as in the corresponding observed sub-sample, where L_p was drawn from the distribution of the observed luminosities in that bin and FWHM_{min} was sampled from a probability density function derived from Gaussian kernel density estimation of the Type-II LGRBs with known redshift. Each point was accepted or rejected based on two conditions: (1) a Bernoulli trial with probability $p = \epsilon_{\text{det}}$ calculated using Eq. (1) for that specific point was successful, and (2) the isotropic energy of this synthetic pulse did not exceed the maximum observed energy in that bin, given by L_p FWHM_{min} $\leq E_{\text{iso,max}}^{(\text{pulse})}$.

We carried out $N = 10^4$ simulations. In this way, we did not assume any correlation between L_p and FWHM_{min}, whereas the resulting apparent correlation is entirely due to the selection effects (Figure 8).

We then applied Pearson, Spearman, and Kendall correlation tests to the real data using logarithmic values for the analysis. For Type-II GRBs, we obtained p-values of 8×10^{-15} , 2.5×10^{-14} , and 8×10^{-13} , respectively. In contrast, we found no evidence of such a correlation for Type-I GRBs, with p-values of 0.96, 0.83, and 0.86, respectively. We then applied the same correlation test to the $N=10^4$ simulated datasets to build the corresponding reference distributions for the p-values that account for the selection effects discussed above. The results are shown in Figure 9 and reveal that the simulated datasets were more correlated than the

real ones only in 0.5%, 2.1%, and 2.3% of cases, respectively, which represent the probabilities that the observed correlation could arise purely from selection effects.

3.5. Number of peaks versus FWHM_{min}

Figure 10 shows FWHM_{min} versus the number of peaks within a GRB. GRBs with numerous peaks (peak-rich GRBs) tend to have shorter MVTs compared with those with fewer peaks (peak-poor GRBs), as was also observed in *Swift*/BAT GRBs (Guidorzi et al. 2016). The same authors also found that peak-richness correlates with a shallower power density spectrum, which means that shorter timescales have relatively more temporal power than in peak-poor GRBs (Guidorzi et al. 2024b).

3.6. Lorentz factor versus FWHM_{min}

We took the Lorentz factors (LFs, hereafter noted as Γ_0) from the same references as in C23, that is Lü et al. (2012), Xue et al. (2019), and Xin et al. (2016). We found 95 GRBs both detected by Fermi/GBM and reported in these studies. For 87 of them, Xue et al. (2019) made use of the $L_{\rm iso}$ – E_p – Γ_0 correlation to get pseudo values of Γ_0 , while for the remaining nine, we used the early afterglow peak to compute Γ_0 . We then considered additional references for individual GRBs: 140102A, whose Γ_0 was reported by Gupta et al. (2021) (who also modelled the forward and reverse shock), as well as 211211A and 230307A. The value of the LF of 211211A (approximately $\Gamma_0 \sim 1000$) has been obtained by modelling the forward shock (Mei et al. 2022) and by measuring the deceleration peak (Veres et al. 2023). According to Zhong et al. (2024), 230307A has $\log(\Gamma_0) \sim 2.77$. Our sample also includes one SGRB, 090510, which is a rare case of SGRB detected by Fermi/LAT. In this case, Γ_0 was estimated from the peak of the high-energy afterglow (Ghirlanda et al. 2010). The other SGRB in our sample is 170817A, for which a considerably less reliable measure of Γ_0 was obtained using $E_{\rm p,i}-E_{\rm iso}$ and $\Gamma_0-E_{\rm iso}$ correlations (Zou et al. 2018). We also considered the sample of GRBs from Ghirlanda et al. (2018) separately. We collected 65 Type-II GRBs in common with our sample, with 26 of them being part of their golden or silver sample and 39 taken as upper limits. We also report the six cases of Type-I GRBs for which a measure of Γ_0 is possible. The results are shown in Figure 11. The left panel shows FWHM_{min} versus Γ_0 , while the right panel displays FWHM_{min} versus Γ_0 as measured by Ghirlanda et al. (2018).

We computed the radius, R, at which the gamma-ray emission is produced using

$$R = 2 c \Gamma_0^2 \text{ FWHM}_{\text{min}} = 6 \times 10^{14} \text{ cm} \left[\frac{\Gamma_0}{100} \right]^2 \left[\frac{\text{FWHM}_{\text{min}}}{1 \text{ s}} \right]. (3)$$

Eq. (3) is derived from the IS model (Rees & Meszaros 1994; Daigne & Mochkovitch 1998). We used FWHM_{min} as a proxy of the MVT in the emission radius calculation rather than Δt_{min} because the former can be considered as the sum of the rise and the decay time, while the latter gives only the rise time. This choice was motivated by the fact that the emission radius in the IS framework is linked to the angular spreading timescale, $R/c\Gamma^2$, which also governs the decay time of the pulse (Kobayashi et al. 2002). Since the decay of GRB pulses is three to four times slower than the rise, it is more accurate to consider FWHM_{min} than Δt_{min} when computing the emission radius. Figure 12 shows the *R* distribution for the Type-II GRBs in our sample. The emission radii, *R*, for all of our GRBs range from

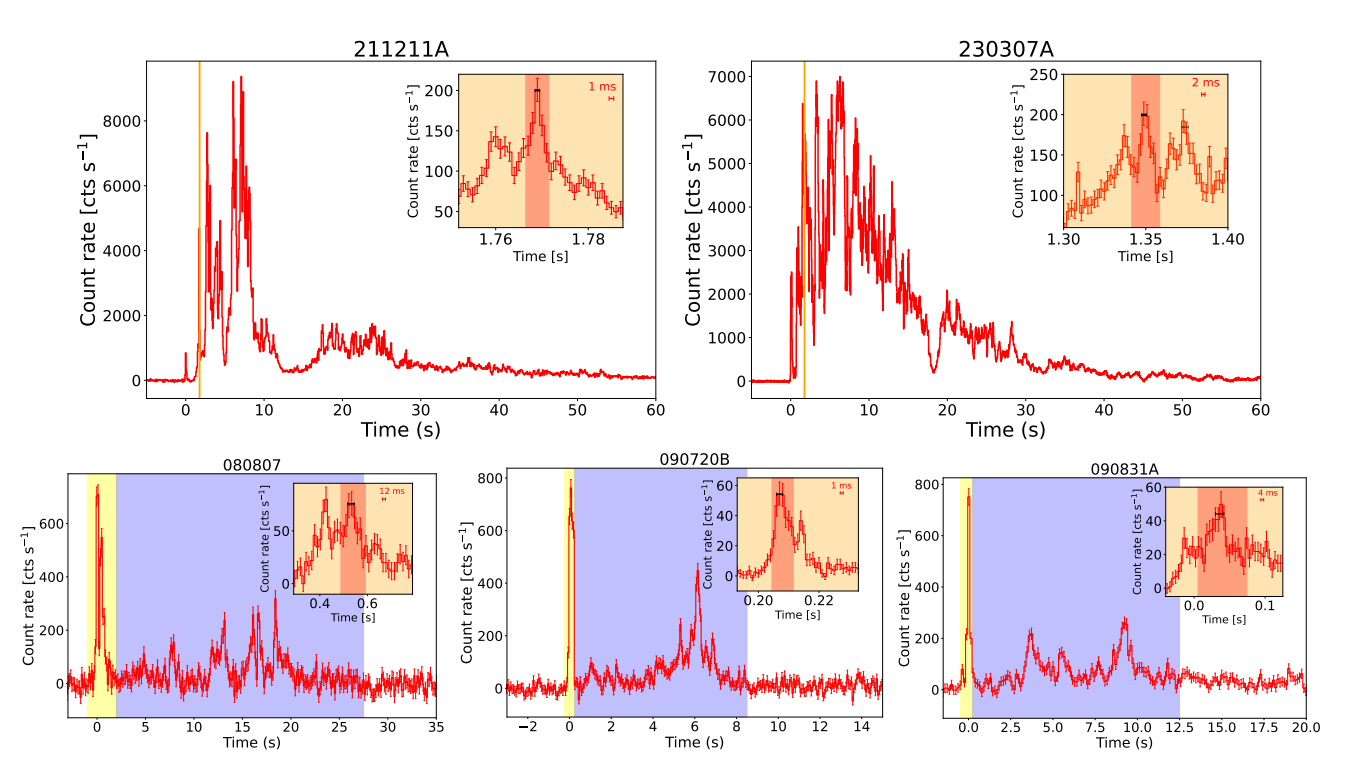


Fig. 5. *Top panels:* LC of 211211A (left) and of 230307A (right) when using the 8–1000 keV range. *Bottom panels, left to right:* LC of 080807, 090720B, and 090832A, respectively (in the same energy range as top panels). The yellow window includes the initial short spike, while the blue one includes the extended emission. The inset in each panel shows a zoom-in on the narrowest pulse. The black point indicates the detection timescale, Δt_{det} , of the narrowest pulse, while the orange region shows the window encompassing FWHM_{min}.

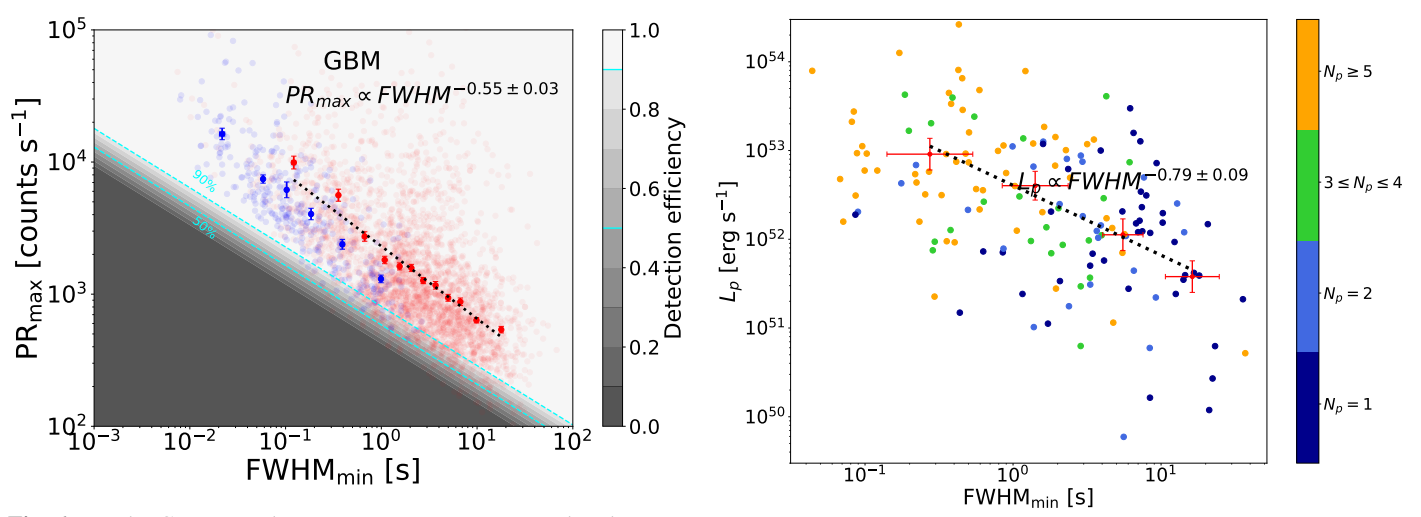


Fig. 6. For the GBM sample, PR_{max} versus $FWHM_{min}$. Blue dots represent Type-I GRBs (i.e. SGRBs and SEE-GRBs), while red dots represent Type-II GRBs. Lighter dots correspond to individual GRB data, and darker dots indicate the geometric mean of data from GRB groups sorted by increasing $FWHM_{min}$. Each Type-I group consists of 50 GRBs; each Type-II group consists of 270 GRBs. Dotted lines show the best fit for Type-II GRBs. Shaded areas illustrate ten regions with a detection efficiency ranging from 0 to 1. Cyan dashed lines indicate the 50% and 90% detection efficiency contours.

 10^{14} to 10^{17} cm. Notably, 80% of the bursts have R values greater than 10^{15} cm, with a mean value of $\sim 6 \times 10^{15}$ cm. As a further test, we computed the deceleration radius, $R_{\rm dec}$, and we checked that $R < R_{\rm dec}$ using

$$R_{\text{dec}} = 6.2 \times 10^{16} \text{ cm} \quad E_{\text{iso,52}}^{1/3} \Gamma_2^{-2/3} n^{-1/3},$$
 (4)

Fig. 7. Peak luminosity versus $FWHM_{min}$ for collapsar-candidate (or Type-II) GRBs. The red points represent the geometric means of GRB groups sorted by increasing $FWHM_{min}$. The dashed line indicates the best fit. GRBs are also categorised by the number of peaks, with the more luminous ones having more peaks.

where $E_{\rm iso,52} = E_{\rm iso}/10^{52}$ erg and $\Gamma_2 = \Gamma/100$, with $E_{\rm iso}$ being the explosion energy ($E_{\rm iso} = E_{\gamma,\rm iso}/\eta$, with efficiency η) and n the medium density. This was derived from Sari & Piran (1999), Molinari et al. (2007) and corresponds to the thin shell case. We assumed a constant density medium of $n = 1 \text{ cm}^{-3}$ and an efficiency of $\eta = 0.2$. We found only two cases where $R > R_{\rm dec}$, namely 090423 and 171222A, with $R/R_{\rm dec}$ ratios of 1.1 and 1.3, respectively. Unfortunately, there is no broadband modelling of the afterglow for these GRBs, so we are

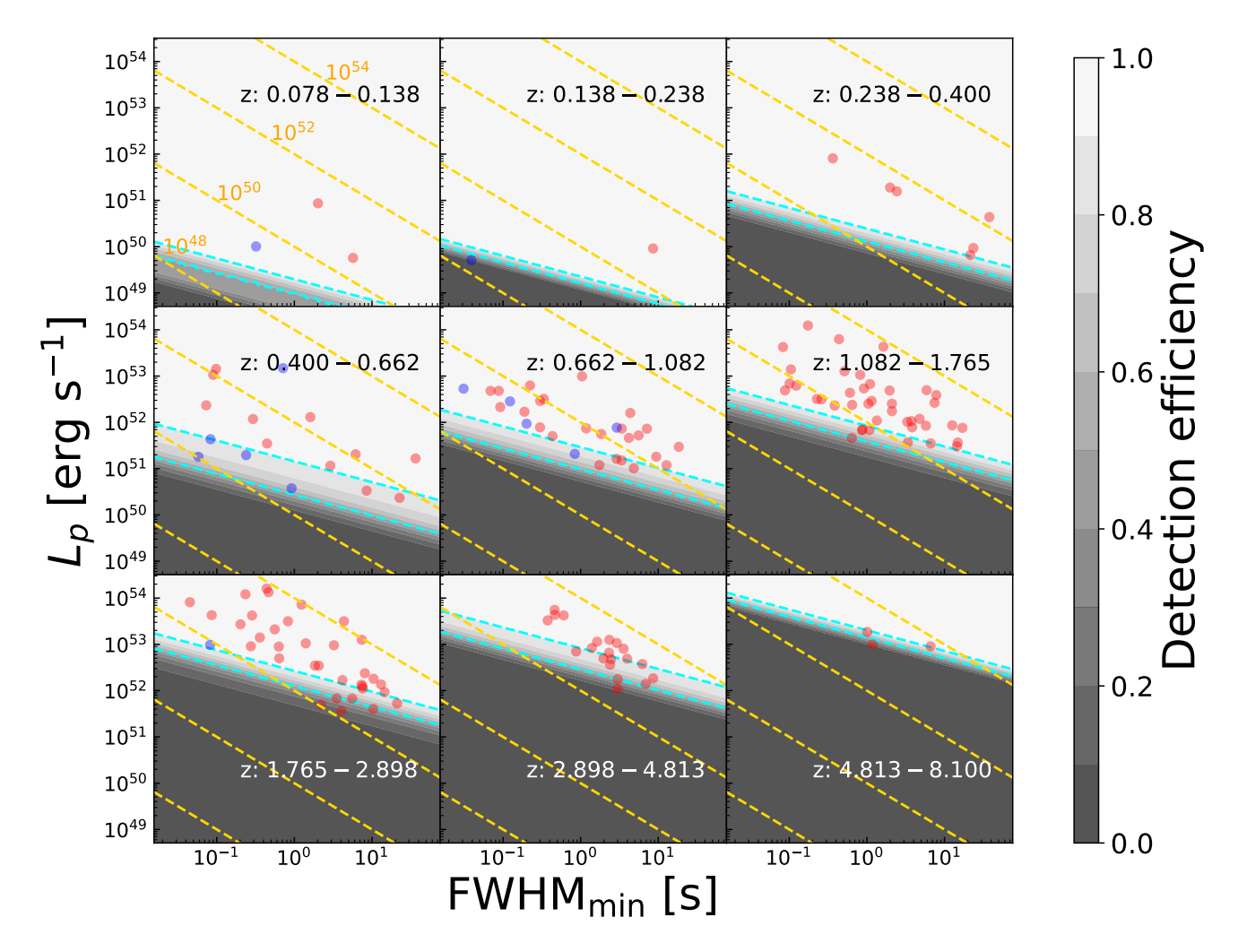


Fig. 8. Diagram showing L_p versus FWHM_{min} for the Fermi/GBM divided into nine redshift bins with equal logarithmic spacing in luminosity distance. The blue dots represent merger-candidates (or Type-I GRBs), and red dots represent collapsar-candidates (or Type-II GRBs). The dashed cyan lines show 90% and 50% detection efficiency (vertical bars). Gold dashed lines indicate regions of constant isotropic-equivalent released energy (in erg) for each peak, roughly calculated as $E_{\rm iso} = L_p \times {\rm FWHM_{min}}$.

unable to verify whether our fiducial values are accurate estimates of the explosion energy and medium density in these cases.

3.7. Peak energy versus FWHM_{min}

We explored the relationship between the MVT and the peak energy, E_p . We took the E_p information from the GBM catalogue (Goldstein et al. 2012). For 1921 bursts, measures of both E_p and FWHM_{min} are available. For a subsample of 107 with measured redshift, we could also compute the rest-frame peak energy $E_{p,i} = (1+z) E_p$. We calculated the Pearson, Spearman, and Kendall correlation coefficients using the logarithmic values, which turned out to be -0.29, -0.30, and -0.21, with associated p-values of $(5, 2.4, \text{ and } 2) \times 10^{-4}$, respectively. This suggests that the two quantities are somehow correlated, despite the large dispersion, as shown in Figure 13.

We fitted the data with a power law, $\log{(E_p/\text{keV})} = m \log{(\text{FWHM}_{\text{min}}/\text{s})} + q$, and modelled the dispersion as a further parameter, minimising the D'Agostini likelihood (D'Agostini 2005). This likelihood is suitable to model correlations affected by a significant scatter, which is treated as a model parameter and is referred to as intrinsic dispersion of the correlation,

denoted with σ . The resulting parameters are $m = -0.19^{+0.10}_{-0.09}$, $q = 2.66 \pm 0.07$, and $\sigma = 0.43^{0.06}_{-0.05}$.

4. Discussion and conclusions

As previously investigated in C23, we confirm that FWHM_{min} is a robust estimate of the MVT, although it carries a slightly different meaning compared to G15, which is more tightly connected to the rise time of the pulse. The MEPSA detection timescale, however, also proves to be a good indicator of the rise time of the narrowest pulse, thus providing a very simple and practical method to compute it. These differences are important to keep in mind, especially when the MVT values are interpreted within a theoretical context.

In the IS model, the hydrodynamic timescale and the angular spreading timescale govern the rise and the decay time of a GRB pulse, respectively (e.g. Kobayashi et al. 2002). The hydrodynamic timescale, which dictates the rise time, is the shock-crossing time, approximately $\sim l/c$, where l represents the characteristic irregularity scale or shell width in the outflow. The angular spreading timescale, which determines the decay time, results from the time delay or spread due to the angular extent of the emission region. This timescale is roughly $R/c\Gamma^2$, where

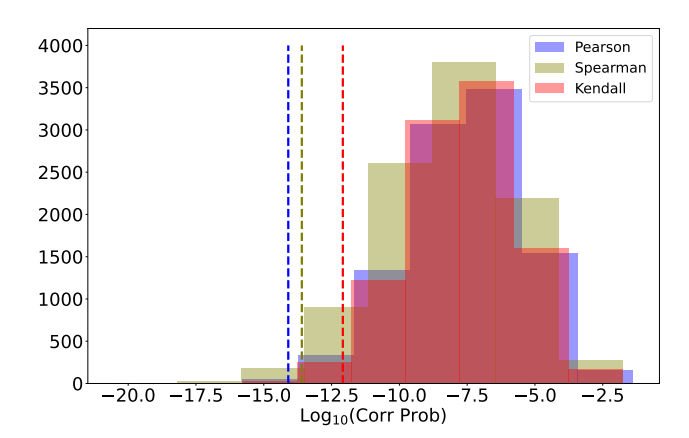


Fig. 9. Pearson, Spearman, and Kendall correlation p-values (in logarithm units) computed on $N=10^4$ simulated samples (blue, olive, and red histograms) compared to the ones computed on the real dataset (blue, olive, and red dashed lines, respectively).

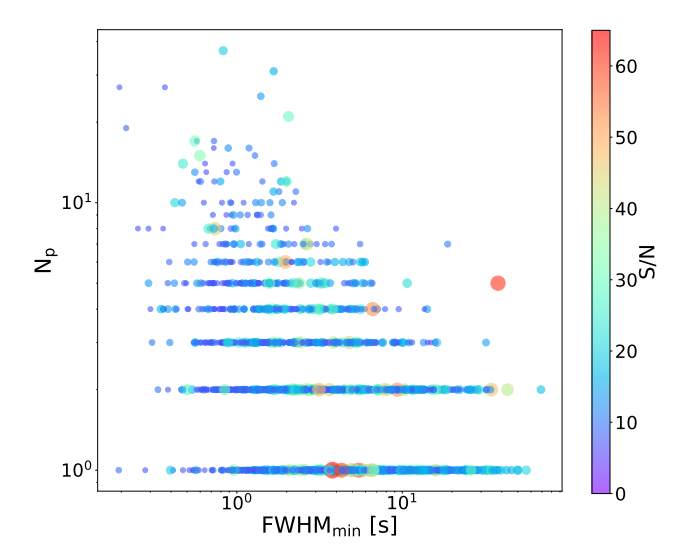


Fig. 10. Number of pulses within a GRB as a function of FWHM_{min} colour-coded by S/N. The GRBs that are composed of a large number of pulses are more likely to have a shorter $FWHM_{min}$.

R is the emission radius and Γ is the Lorentz factor of the emission region. Since most observed pulses exhibit a faster rise than decay, the pulse width is primarily set by the angular spreading time.

We confirm that millisecond-long pulses are very rare in GRBs. While partly affected by detection thresholds, their scarcity appears to be a genuine feature. Having investigated three independent studies, we confirm that SEE-GRBs have shorter MVTs than LGRBs, compatible with the bulk of SGRBs. Additionally, the three well-known long-duration merger candidates 211211A, 230307A, and 191019A to a lesser extent have very short MVTs (5, 17, and 150 ms), providing further evidence that short MVTs are characteristic of Type-I GRBs, regardless of the total duration. Our MVT results align with the conventional interpretation that SEE-GRBs are essentially SGRBs with an additional emission component. The exact physical mechanism behind the extended emission remains unclear. Several models have been proposed, including long-lasting activity from the central engine, such as a magnetar formed during the merger (Metzger et al. 2008; Jordana-Mitjans et al. 2022) or energy release from a late fallback accretion disc (Rosswog 2007; Musolino et al. 2024), both of which can continue powering the emission after the main burst. These results emphasise the importance of multi-wavelength follow-up observations, particularly for LGRBs with low MVTs, as these could reveal other merger events that might otherwise be misclassified as collapsar candidates.

The differences in MVT between Type-I and Type-II GRBs may indicate distinct progenitors or disparities in jet propagation. The irregularity in GRB jets arises from a combination of internal factors, such as variability in the central engine, and external factors such as interaction with the surrounding medium and jet instabilities. The conventional central engines are magnetars or black hole accretion disc systems. Even if both types of GRBs are powered by black hole accretion discs, the black holes in Type I events (SGRBs) likely have smaller masses, resulting in shorter dynamical timescales. The GRB jets must also penetrate a dense medium surrounding the central engines: a stellar envelope in the case of LGRBs (Type II) or neutron star merger ejecta in the case of SGRBs (Type I). This interaction fosters the growth of hydrodynamic instabilities along the jet boundary (e.g. Gottlieb et al. 2020). Type II jets are likely more unstable due to the higher density of the surrounding stellar envelope. Additionally, pulses emitted within the photospheric radius are obscured, adding further complexity. Extragalactic MGFs have an even shorter MVT than every GRB population, thus offering an additional tool to distinguish them from traditional GRB events.

We have confirmed, using an independent dataset, that in the case of Type-II GRBs, peak luminosity does correlate with FWHM_{min}, while the same does not hold true for Type-I GRBs. The question as to whether this is a result of a much poorer sample or due to the intrinsic absence of correlation will be addressed through future richer datasets. We confirmed that GRBs with many pulses (pulse-rich GRBs, as defined in Guidorzi et al. 2024b) tend to have shorter MVTs, supporting the presence of two temporal behaviours: rapid variability atop a slower FRED-like envelope and purely slow, FRED-like evolution. This distinction may reflect differences in central engine activity, circumburst interactions, or progenitor type. We computed the LF and source emission radius, R. The R values we found generally do not align with the IS model, where R typically ranges from 10^{13} to 10^{14} cm. However, they are consistent with the ICMART model, which predicts gamma-ray emission at larger radii, $R > 10^{15-16}$ cm (Zhang & Yan 2011), through magnetic reconnection cascades.

We have investigated the plausible correlation between MVT and peak energy. Given the established anti-correlation between MVT and peak luminosity (see also C23, Wu et al. 2016) and the known correlation between peak energy and peak luminosity (Yonetoku et al. 2004; Ghirlanda et al. 2005), in principle, we expected an anti-correlation between the MVT and $E_{p,i}$. Moreover, several GRBs with a small MVT have also been detected at higher energies by Fermi/LAT, such as 080916C (0.3 s, Tajima et al. 2008); 090510 (0.011 s, Ohno & Pelassa 2009); 090720B (0.014 s, Rubtsov et al. 2012); and 210410A (0.07 s, Arimoto et al. 2021). Although we do find a correlation, it is very dispersed. Smaller MVTs may imply shorter angular spreading times and smaller emission radii, resulting in higher shock energy density in the emission region. In the standard synchrotron shock model, a constant fraction of the shock energy is transferred to magnetic fields, with radiation from smaller radii generally expected to be harder. However, since both the shock energy generated through internal dissipation and the blue-shift of emission frequencies depend on the Lorentz factor, velocity

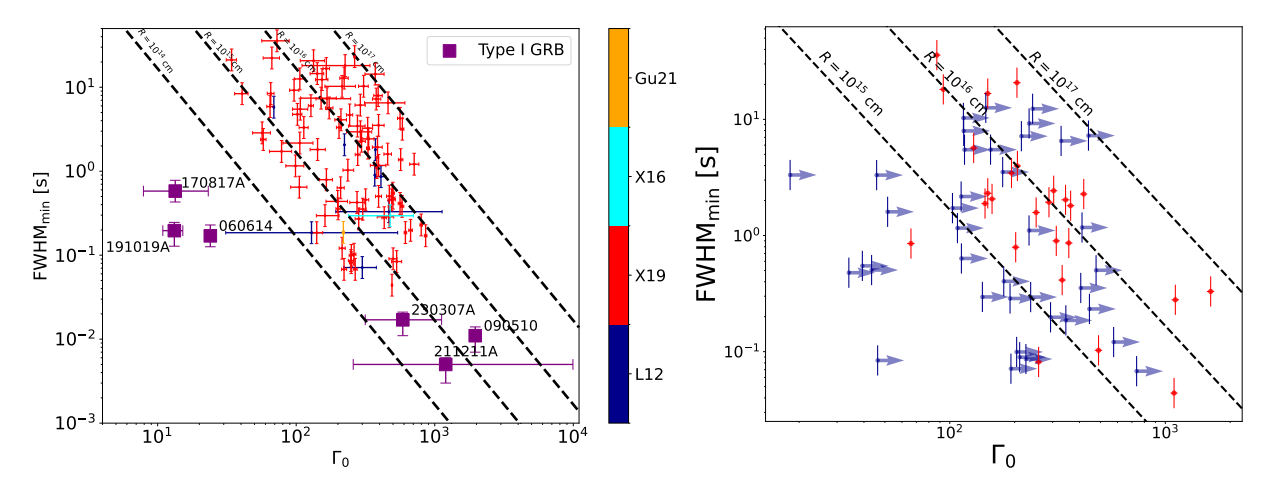


Fig. 11. For the Type-II (red dots) and Type-I GRBs (purple squares) present in our sample, FWHM_{min} versus the initial Lorentz factor Γ_0 . In the left panel, the Γ_0 values are from different datasets and colour-coded as follows: L12 Lü et al. (2012), X19 Xue et al. (2019), X16 Xin et al. (2016), and Gu21 Gupta et al. (2021). The dashed lines represent the typical distance $R = 2c\Gamma_0^2$ FWHM_{min} where the dissipation process responsible for the prompt emission could occur. The right panel is the same as the left, but Γ_0 has been calculated using the dataset from Ghirlanda et al. (2018). Red points indicate GRBs from their golden and silver samples, while blue points represent lower limits on Γ_0 .

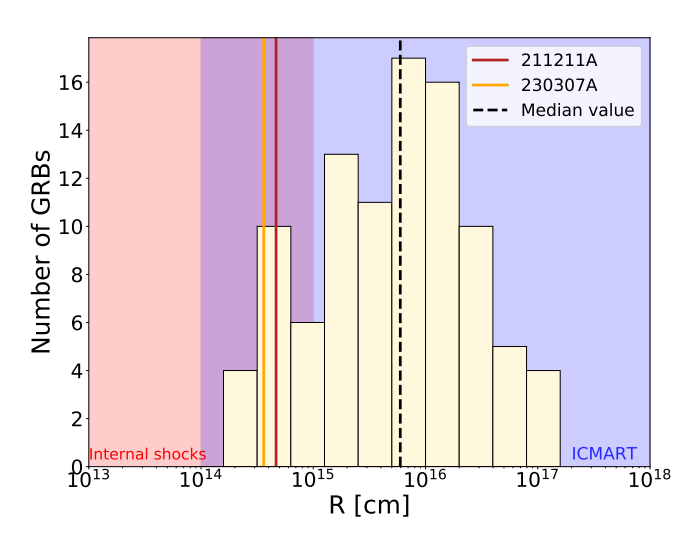


Fig. 12. Source emission region radii for the GBM sample. The red and orange vertical lines represent the value of this radius for 211211A and 230307A, while the dashed vertical line represents the median value of the distribution. The red shaded regions indicate the values expected by the IS model ($10^{13}~{\rm cm} \lesssim R \lesssim 10^{15}~{\rm cm}$; Rees & Meszaros 1994; Daigne & Mochkovitch 1998), while the blue one indicates the expectations for the ICMART model ($R \gtrsim 10^{14-15}~{\rm cm}$; Zhang & Yan (2011)). In the decade $10^{14-15}~{\rm cm}$ (purple), the two regions overlap, and the emission radii in this region are marginally compatible with both models.

irregularities in the outflow-an essential assumption of the IS model-can introduce significant dispersion in this relationship.

5. Data availability

Table 1 is available at the CDS via https://cdsarc.cds.unistra.fr/viz-bin/cat/J/A+A/702/A95.

Acknowledgements. We are grateful to the anonymous reviewer for their precious report which helped us to cross-check our results and to overall improve the quality of this work. R.M. and M.M. acknowledge the University of Ferrara for the financial support of their PhD scholarships. L.F. acknowledges support from the AHEAD-2020 Project grant agreement 871158 of the European Union's Horizon 2020 Program. A.T. acknowledges financial support from ASI-

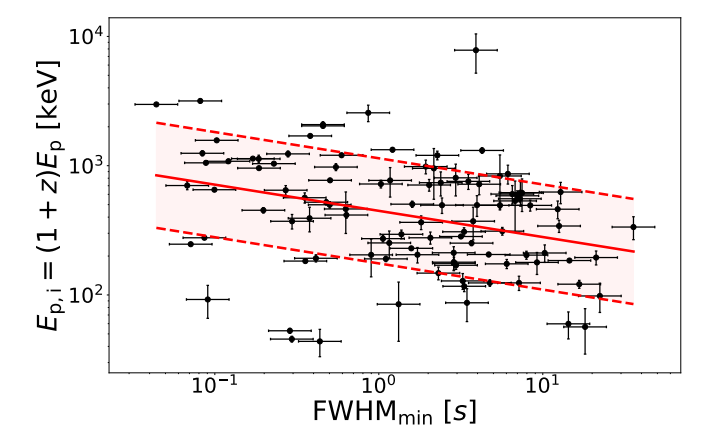


Fig. 13. For all Type-II GRBs with known redshift, $E_{p,i}$ versus FWHM_{min}. The solid red line shows the best fit, while the two dashed red lines show the dispersion of the correlation.

INAF Accordo Attuativo HERMES Pathfinder operazioni n. 2022-25-HH.0 and the basic funding program of the Ioffe Institute FFUG-2024-0002. L.A. acknowledges support from INAF Mini-grant programme 2022. A.E.C received support from the European Research Council (ERC) via the ERC Synergy Grant ECO-GAL (grant 855130). Views and opinions expressed by ERC-funded scientists are however those of the author(s) only and do not necessarily reflect those of the European Union or the European Research Council. Neither the European Union or the granting authority can be held responsible for them. M. B. acknowledges the Department of Physics and Earth Science of the University of Ferrara for the financial support through the FIRD 2024 grant.

References

Ackermann, M., Ajello, M., Asano, K., et al. 2014, Science, 343, 42
Arimoto, M., Ohno, M., Longo, F., Axelsson, M., & Fermi-LAT Team 2021, GRB Coordinates Network, 29781, 1
Bhat, P. N., Briggs, M. S., Connaughton, V., et al. 2012, ApJ, 744, 141
Blinnikov, S. I., Novikov, I. D., Perevodchikova, T. V., & Polnarev, A. G. 1984, Sov. Astron. Lett., 10, 177
Bulla, M., Camisasca, A. E., Guidorzi, C., et al. 2023, GRB Coordinates Network, 33578, 1
Burns, E., Svinkin, D., Hurley, K., et al. 2021, ApJ, 907, L28
Camisasca, A. E., Guidorzi, C., Amati, L., et al. 2023a, A&A, 671, A112

Abbott, B. P., Abbott, R., Abbott, T. D., et al. 2017, ApJ, 848, L13

```
Camisasca, A. E., Guidorzi, C., Bulla, M., et al. 2023b, GRB Coordinates
                                                                                      MacLachlan, G. A., Shenoy, A., Sonbas, E., et al. 2013, MNRAS, 432, 857
                                                                                      Mazets, E. P., Golentskii, S. V., Ilinskii, V. N., Aptekar, R. L., & Guryan, I. A.
   Network, 33577, 1
Chen, J.-M., Zhu, K.-R., Peng, Z.-Y., & Zhang, L. 2024, MNRAS, 527, 4272
                                                                                          1979, Nature, 282, 587
D'Agostini, G. 2005, ArXiv e-prints [arXiv: physics/0511182]
                                                                                      Mazets, E. P., Aptekar, R. L., Cline, T. L., et al. 2008, ApJ, 680, 545
Dai, C.-Y., Guo, C.-L., Zhang, H.-M., Liu, R.-Y., & Wang, X.-Y. 2024, ApJ, 962,
                                                                                      Meegan, C., Lichti, G., Bhat, P. N., et al. 2009, ApJ, 702, 791
                                                                                       Mei, A., Banerjee, B., Oganesyan, G., et al. 2022, Nature, 612, 236
Daigne, F., & Mochkovitch, R. 1998, MNRAS, 296, 275
                                                                                       Mereghetti, S., Rigoselli, M., Salvaterra, R., et al. 2024, Nature, 629, 58
Della Valle, M., Chincarini, G., Panagia, N., et al. 2006, Nature, 444, 1050
                                                                                      Metzger, B. D., Quataert, E., & Thompson, T. A. 2008, MNRAS, 385, 1455
Di Matteo, T., Perna, R., & Narayan, R. 2002, ApJ, 579, 706
                                                                                       Metzger, B. D., Giannios, D., Thompson, T. A., Bucciantini, N., & Quataert, E.
Dimple, Misra, K., & Arun, K. G. 2023, ApJ, 949, L22
                                                                                         2011, MNRAS, 413, 2031
Dimple, Misra, K., & Arun, K. G. 2024, ApJ, 974, 55
                                                                                       Minaev, P. Y., Pozanenko, A. S., Grebenev, S. A., et al. 2024, Astron. Lett., 50, 1
Du, Z., Lü, H., Yuan, Y., Yang, X., & Liang, E. 2024, ApJ, 962, L27
Eichler, D., Livio, M., Piran, T., & Schramm, D. N. 1989, Nature, 340, 126
                                                                                       Molinari, E., Vergani, S. D., Malesani, D., et al. 2007, A&A, 469, L13
                                                                                       Musolino, C., Duqué, R., & Rezzolla, L. 2024, ApJ, 966, L31
Fenimore, E. E., in 't Zand, J. J. M., Norris, J. P., Bonnell, J. T., & Nemiroff, R.
                                                                                      Narayan, R., Paczynski, B., & Piran, T. 1992, ApJ, 395, L83
   1989, ApJ, 448, L101
                                                                                       Norris, J. P., & Bonnell, J. T. 2006, ApJ, 643, 266
Dalessi, S., Roberts, O. J., Meegan, C., & Fermi GBM Team 2023, GRB
                                                                                      Norris, J. P., Nemiroff, R. J., Bonnell, J. T., et al. 1996, ApJ, 459, 393
   Coordinates Network, 33411, 1
                                                                                       Norris, J. P., Bonnell, J. T., Kazanas, D., et al. 2005, ApJ, 627, 324
Fermi-Lat Collaboration 2021, Nat. Astron., 5, 385
                                                                                      Ofek, E. O., Kulkarni, S. R., Nakar, E., et al. 2006, ApJ, 652, 507
Feroci, M., Frontera, F., Costa, E., et al. 1999, ApJ, 515, L9
                                                                                       Ohno, M., & Pelassa, V. 2009, GRB Coordinates Network, 9334, 1
                                                                                      Paczynski, B. 1986, ApJ, 308, L43
Fruchter, A. S., Levan, A. J., Strolger, L., et al. 2006, Nature, 441, 463
Fynbo, J. P. U., Watson, D., Thöne, C. C., et al. 2006, Nature, 444, 1047
                                                                                      Paczynski, B. 1991, Acta Astron., 41, 257
Galama, T. J., Vreeswijk, P. M., van Paradijs, J., et al. 1998, Nature, 395, 670
                                                                                      Paczyński, B. 1998, ApJ, 494, L45
                                                                                      Planck Collaboration VI. 2020, A&A, 641, A6
Garcia-Cifuentes, K., Becerra, R. L., De Colle, F., Cabrera, J. I., & Del Burgo,
                                                                                      Popham, R., Woosley, S. E., & Fryer, C. 1999, ApJ, 518, 356
   C. 2023, ApJ, 951, 4
Gehrels, N., Norris, J. P., Barthelmy, S. D., et al. 2006, Nature, 444, 1044
                                                                                      Rastinejad, J. C., Gompertz, B. P., Levan, A. J., et al. 2022, Nature, 612, 223
Ghirlanda, G., Ghisellini, G., & Firmani, C. 2005, MNRAS, 361, L10
                                                                                      Rees, M. J., & Meszaros, P. 1994, ApJ, 430, L93
Ghirlanda, G., Ghisellini, G., & Nava, L. 2010, A&A, 510, L7
                                                                                      Roberts, O. J., Veres, P., Baring, M. G., et al. 2021, Nature, 589, 207
Ghirlanda, G., Nappo, F., Ghisellini, G., et al. 2018, A&A, 609, A112
                                                                                      Rodi, J. C., Pacholski, D. P., Mereghetti, S., et al. 2025, ApJ, 979, L25
Goldstein, A., Preece, R. D., & Briggs, M. S. 2010, ApJ, 721, 1329
                                                                                       Rosswog, S. 2007, MNRAS, 376, L48
Goldstein, A., Burgess, J. M., Preece, R. D., et al. 2012, ApJS, 199, 19
                                                                                      Rubtsov, G. I., Pshirkov, M. S., & Tinyakov, P. G. 2012, MNRAS, 421, L14
Goldstein, A., Cleveland, W. H., & Kocevski, D. 2022, Fermi GBM Data Tools:
                                                                                      Salmon, L., Hanlon, L., & Martin-Carrillo, A. 2022, Galaxies, 10, 78
                                                                                       Sari, R., & Piran, T. 1999, ApJ, 520, 641
                                                                                       Scargle, J. D., Norris, J. P., Jackson, B., & Chiang, J. 2013, ApJ, 764, 167
Golkhou, V. Z., & Butler, N. R. 2014, ApJ, 787, 90
Golkhou, V. Z., Butler, N. R., & Littlejohns, O. M. 2015, ApJ, 811, 93
                                                                                       Steinhardt, C. L., Mann, W. J., Rusakov, V., & Jespersen, C. K. 2023, ApJ, 945,
Gompertz, B. P., Ravasio, M. E., Nicholl, M., et al. 2023, Nat. Astron., 7, 67
Gottlieb, O., Bromberg, O., Singh, C. B., & Nakar, E. 2020, MNRAS, 498, 3320
                                                                                      Stratta, G., Nicuesa Guelbenzu, A. M., Klose, S., et al. 2025, ApJ, 979, 159
Guidorzi, C. 2015, Astron. Comput., 10, 54
                                                                                       Svinkin, D., Frederiks, D., Hurley, K., et al. 2021, Nature, 589, 211
Guidorzi, C., Dichiara, S., & Amati, L. 2016, A&A, 589, A98
                                                                                       Tajima, H., Bregeon, J., Chiang, J., & Thayer, G. 2008, GRB Coordinates
Guidorzi, C., Maccary, R., Tsvetkova, A., et al. 2024a, A&A, 690, A261
                                                                                         Network, 8246, 1
                                                                                       Thompson, T. A., Chang, P., & Quataert, E. 2004, ApJ, 611, 380
Guidorzi, C., Sartori, M., Maccary, R., et al. 2024b, A&A, 685, A34
Gupta, R., Oates, S. R., Pandey, S. B., et al. 2021, MNRAS, 505, 4086
                                                                                      Trigg, A. C., Burns, E., Roberts, O. J., et al. 2024, A&A, 687, A173
Hjorth, J., Sollerman, J., Møller, P., et al. 2003, Nature, 423, 847
                                                                                      Troja, E., Fryer, C. L., O'Connor, B., et al. 2022, Nature, 612, 228
                                                                                      Tsvetkova, A., Amati, L., Bulla, M., et al. 2025, A&A, 698, A169
Hurley, K., Cline, T., Mazets, E., et al. 1999, Nature, 397, 41
Hurley, K., Boggs, S. E., Smith, D. M., et al. 2005, Nature, 434, 1098
                                                                                      Usov, V. V. 1992, Nature, 357, 472
                                                                                       Veres, P., Bhat, P. N., Burns, E., et al. 2023, ApJ, 954, L5
Janiuk, A., Yuan, Y., Perna, R., & Di Matteo, T. 2007, ApJ, 664, 1011
Jespersen, C. K., Severin, J. B., Steinhardt, C. L., et al. 2020, ApJ, 896, L20
                                                                                       Vianello, G., Gill, R., Granot, J., et al. 2018, ApJ, 864, 163
Jin, Z.-P., Li, X., Cano, Z., et al. 2015, ApJ, 811, L22
                                                                                       Wheeler, J. C., Yi, I., Höflich, P., & Wang, L. 2000, ApJ, 537, 810
Jordana-Mitjans, N., Mundell, C. G., Guidorzi, C., et al. 2022, ApJ, 939,
                                                                                       Woosley, S. E. 1993, ApJ, 405, 273
                                                                                       Wu, Q., Zhang, B., Lei, W.-H., et al. 2016, MNRAS, 455, L1
                                                                                      Xiao, S., Peng, W.-X., Zhang, S.-N., et al. 2022, ApJ, 941, 166
Kaneko, Y., Bostancı, Z. F., Göğüş, E., & Lin, L. 2015, MNRAS, 452, 824
                                                                                       Xin, L.-P., Wang, Y.-Z., Lin, T.-T., et al. 2016, ApJ, 817, 152
Kobayashi, S., Piran, T., & Sari, R. 1997, ApJ, 490, 92
Kobayashi, S., Ryde, F., & MacFadyen, A. 2002, ApJ, 577, 302
                                                                                       Xiong, S., Wang, C., & Huang, Y. Gecam Team 2023, GRB Coordinates
Kumar, P., & Narayan, R. 2009, MNRAS, 395, 472
                                                                                         Network, 33406, 1
Lan, L., Lu, R.-J., Lü, H.-J., et al. 2020, MNRAS, 492, 3622
                                                                                      Xue, L., Zhang, F.-W., & Zhu, S.-Y. 2019, ApJ, 876, 77
Yang, B., Jin, Z.-P., Li, X., et al. 2015, Nat. Commun., 6, 7323
Lei, W.-H., Zhang, B., & Liang, E.-W. 2013, ApJ, 765, 125
Lesage, S., Veres, P., Briggs, M. S., et al. 2023, ApJ, 952, L42
                                                                                       Yang, J., Chand, V., Zhang, B.-B., et al. 2020, ApJ, 899, 106
Levan, A. J., Malesani, D. B., Gompertz, B. P., et al. 2023, Nat. Astron., 7, 976
                                                                                       Yang, J., Ai, S., Zhang, B. B., et al. 2022, Nature, 612, 232
Levan, A. J., Gompertz, B. P., Salafia, O. S., et al. 2024, Nature, 626, 737
                                                                                       Yang, Y.-H., Troja, E., O'Connor, B., et al. 2024, Nature, 626, 742
Lien, A., Sakamoto, T., Barthelmy, S. D., et al. 2016, ApJ, 829, 7
Lü, H.-J., Liang, E.-W., Zhang, B.-B., & Zhang, B. 2010, ApJ, 725, 1965
                                                                                      Yonetoku, D., Murakami, T., Nakamura, T., et al. 2004, ApJ, 609, 935
Yoon, S. C., & Langer, N. 2005, A&A, 443, 643
Zhang, B. 2006, Nature, 444, 1010
Lü, J., Zou, Y.-C., Lei, W.-H., et al. 2012, ApJ, 751, 49
Lü, H.-J., Zhang, B., Liang, E.-W., Zhang, B.-B., & Sakamoto, T. 2014,
                                                                                      Zhang, B., & Yan, H. 2011, ApJ, 726, 90
                                                                                       Zhang, W.-L., Xue, W.-C., Li, C.-K., et al. 2025, ApJ, 986, 170
                                                                                      Zhong, S.-Q., Li, L., Xiao, D., et al. 2024, ApJ, 963, L26
Zhu, S.-Y., Sun, W.-P., Ma, D.-L., & Zhang, F.-W. 2024, MNRAS, 532, 1434
Lyutikov, M., Pariev, V. I., & Blandford, R. D. 2003, ApJ, 597, 998
Maccary, R., Guidorzi, C., Amati, L., et al. 2024, ApJ, 965, 72
MacFadyen, A. I., & Woosley, S. E. 1999, ApJ, 524, 262
                                                                                      Zou, Y.-C., Wang, F.-F., Moharana, R., et al. 2018, ApJ, 852, L1
```

Appendix A: FWHM_{min} compared to a direct fit of the narrowest pulse

We compared FWHM_{min} measurements obtained using MEPSA calibration and the procedure described in C23 with the results derived from fitting the LC with FRED shaped pulses (denoted as FWHM_{fit}; see Maccary et al. (2024) for a detailed description of the technique). To do so, we analysed a sub-sample of GRBs with either one or a few peaks, for which a direct and accurate modelling of the pulses' shapes and FWHMs was feasible. We initially selected 639 single-peaked GRBs with S/N > 10. We excluded the GRBs that displayed a more complex temporal structure than a single well-shaped pulse, ending up with 544 GRBs. Their pulses were then fitted with a FRED template and discarded the cases, whose best-fit parameters were too close to the boundaries (chosen to avoid unrealistic parameter values), or with relative errors on the rise time greater than 50%, reducing the sample to 410 GRBs. We used Swift/BAT data as well, taking a sub-sample of GRBs with less than 8 peaks in their LC. After intersecting these data with the G15 and V23 results, we retained 244 GRBs in the GBM sample and 28 in the BAT sample for a comparative analysis. In Fig. A.1 we illustrated the comparison between FWHM_{min} and FWHM_{fit}, showing how closely the two methods agree across different GRBs. As we can see, for most peaks, $\frac{\text{FWHM}_{\text{fit}}}{2} \leq \text{FWHM}_{\text{min}} \leq 2 \cdot \text{FWHM}_{\text{fit}}$; more precisely, 90% of events are in the range $0.66 \cdot \text{FWHM}_{\text{fit}} \leq \text{FWHM}_{\text{min}} \leq$ $1.92 \cdot \text{FWHM}_{\text{fit}}$.

We furthermore performed a linear fit of the form y = mx + q, applied to the logarithmic values, modelling the intrinsic dispersion $\sigma_{\rm int}$ as a further parameter, adopting the D'Agostini likelihood (D'Agostini 2005). Optimising the parameters using MCMC, we found $m = 0.990^{+0.011}_{-0.004}$, $q = 0.051^{+0.016}_{-0.017}$, and $\sigma_{\rm int} = 0.071^{+0.023}_{-0.028}$. The uncertainty on log FWHM_{min}, previously estimated as $\sigma_{\rm min} = 0.13$ (i.e a 35% relative error on FWHM_{min}), leads to a total uncertainty, accounting for the intrinsic dispersion $\sigma_{\rm int}$, of $\sigma_{\rm tot} = \sqrt{\sigma_{\rm min}^2 + \sigma_{\rm int}^2} \simeq 0.07$ (41%). This implies that the relative error made when using FWHM_{min} instead of FWHM_{fit} is approximately 41%, as opposed to the 35% estimated on synthetic LCs by Camisasca et al. (2023a). This comparison ensures the robustness of our MVT measurements by validating them against an established LC fitting method.

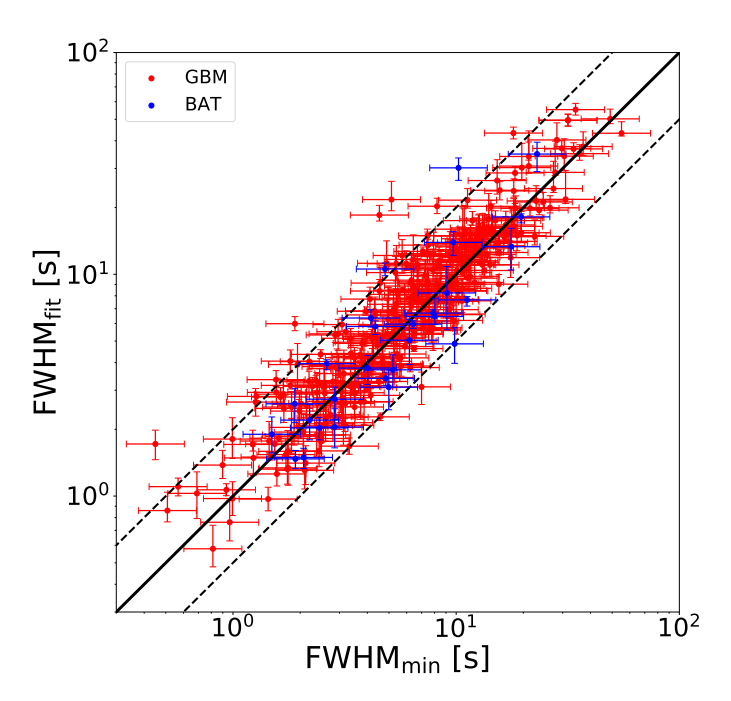


Fig. A.1. Plot presenting FWHM_{min} computed either by following the method described in C23, or by directly fitting the narrowest pulse by a Norris function (called here FWHM_{fit}). Red (blue) points were obtained using GBM (resp. BAT) data. The black line indicates the equality line while the dashed lines show a factor 2 of discrepancy, illustrating that most measurements fall within this range.

Appendix B: Comparison between BAT and GBM

We compared the results obtained by C23 with BAT data with those obtained in this work with GBM data. The FWHM_{min} obtained with the GBM is in mean twice as small as those obtained with the BAT. This was expected due to the dependance of the MVT on the energy band. We also carried this analysis restricting the GBM energy range to the *Swift/BAT* one (15-150 keV). The results show a dispersion around the equality line but no general trend, indicating that our results are consistent with the ones of C23. The results of these two analyses are shown in Figure B.1.

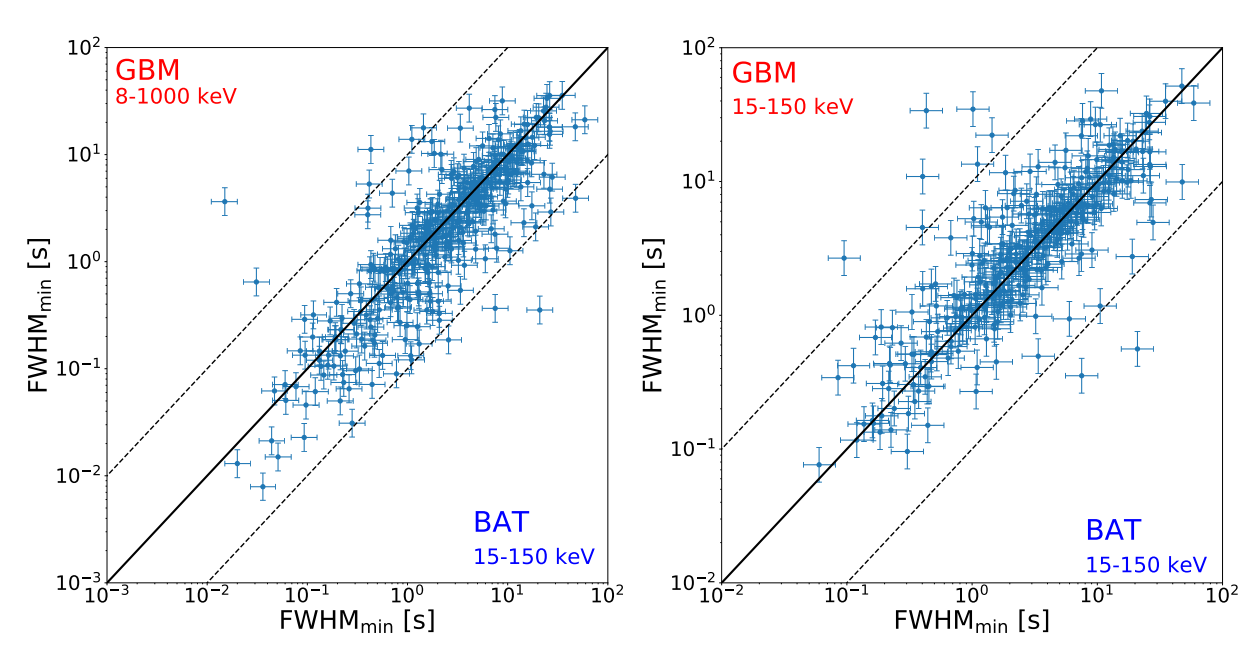


Fig. B.1. Left: FWHM_{min} computed by C23 with BAT data on 15-150 keV against the FWHM_{min} of the same bursts but computed in this work on GBM data on the 8-1000 keV range. Right: Same but the GBM energy range is restricted to 15-150 keV to be the same as BAT.

Appendix C: $FWHM_{min}$ compared with Bayesian blocks

In this section, we compared our results with those obtained by segmenting the LC using Bayesian blocks⁴ (BBs, Scargle et al. 2013). We applied BBs, using a false alarm threshold of p_0 = 10^{-3} to a sample of 96 GRBs, chosen with FWHM_{min} < 50 ms. This choice was made to obtain enough GRBs to make a sound statistical analysis and to include bright GRBs with evident sub-second structures with exquisite S/N. This sample includes, for instance, GRBs as 211211A, 230307A, 190114C, and others known for their rapid temporal variability and brightness, making them ideal test cases. We computed the MVT using BBs, defining it as the shortest block in the segmentation, ΔT_{BB} . Figure C.1 compares these values with those from the MEPSAbased approach. The points scatter around the equality line without a clear systematic bias in either direction. The distribution of the ratio ΔT_{BB} /FWHM_{min} is shown in Fig. C.2 with a median of about 1.03-meaning that, on average, BBs yield MVT values $\sim 3\%$ larger than those obtained with MEPSA. The 90 % confidence interval is [0.4-2.3], meaning that for most GRBs, the discrepancy between the MVTs obtained using BBs and those obtained using MEPSA is smaller than a factor of 2. We further estimated that in roughly 60% cases, the temporal structures identified by MEPSA and BBs coincide; in such cases the discrepancies in MVT values arise only from different ways of estimating the width. BBs, which approximate the pulse as a rectangle, tend to overestimate the width, whereas MEPSA uses a more realistic, though simplified, pulse shape.

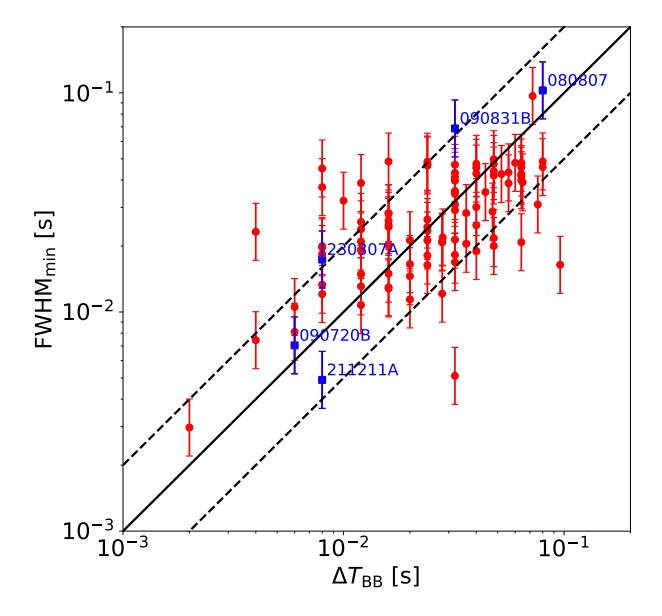


Fig. C.1. Plot of FWHM_{min} versus the shortest segment of the BBs segmentation, ΔT_{BB} . Blue points represents the GRBs shown in Fig. 5.

⁴ We used the function *bayesian_blocks* from the *astropy.stats* python library.

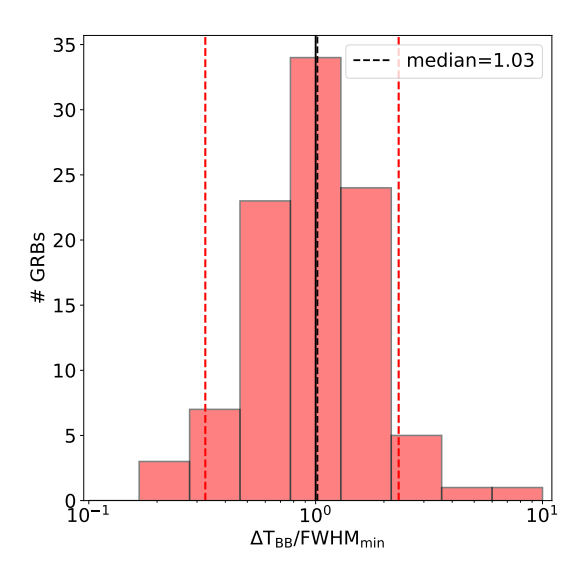


Fig. C.2. Distribution of the ratio ΔT_{BB} over FWHM_{min}. The solid black line represents the case FWHM_{min} = ΔT_{BB} , while the dashed one shows the median value. The two red dashed lines enclose the 90 % confidence interval [0.4-2.3].

Appendix D: Dependence of FWHM_{min} on energy

We computed FWHM_{min} as a function of the geometric mean of the energy range boundaries, for six different energy ranges: 8-30, 8-90, 30-90, 8-1000, 90-300, and 90-1000 keV. We carried out this analysis on 286 bursts, each having a measured FWHM_{min} with S/N > 7 across all six energy ranges. We found that FWHM_{min} \propto E^{- α} with $\alpha_{\rm mean} = 0.46 \pm 0.19$, with a standard dispersion of $\sigma = 0.7$, and $\alpha_{\rm median} = 0.26 \pm 0.12$. Results are shown in Figure D.1. The results are consistent with those of C23 that obtained $\alpha_{\rm mean} = 0.45 \pm 0.08$, $\alpha_{\rm median} = 0.54 \pm 0.07$ and those of Fenimore et al. (1989): $\alpha \in [0.37; 0.46]$.

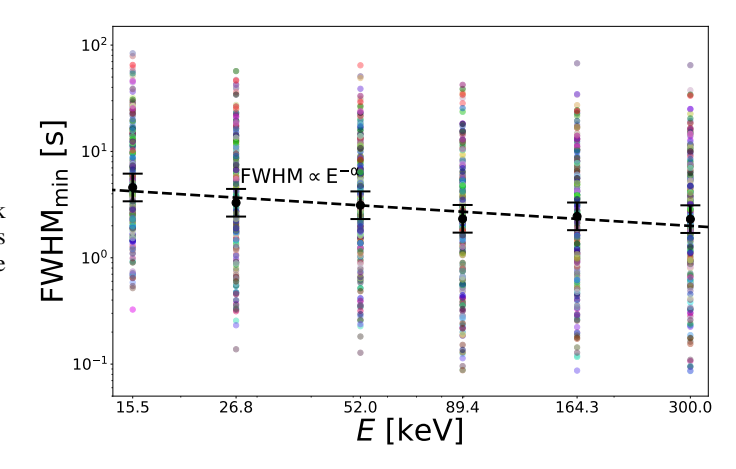


Fig. D.1. Plot showing FWHM_{min} as a function of the geometric mean of the energy range boundaries. The coloured dots are the FWHM_{min} of 286 bursts in four different energy ranges: 8-30, 8-90, 30-90, 8-1000, 90-300, and 90-1000 keV. The values on the x-axis are the geometric means of the corresponding energy boundaries. Black dots with error bars are the weighted averages of the FWHM_{min} for each energy range and the black dashed line is the power-law that best fit the black points.